Thermal induced noise on test mass with copper alloy electrode housing for spaceborne gravitational wave detection

Guilin Li,[1] Jun Ke,[2] Honggang Li,[1] Jie Luo,[2] Li Liu,[1,*] Yiqiu Ma,[1] Shaobo Qu,[1] Xingda Su,[1] Dingyin Tan,[3] Hang Yin,[1] Yujie Zhao,[1] and Zebing Zhou[1,†]

[1]*Centre for Gravitational Experiments, School of Physics, MOE Key Laboratory of Fundamental Physical Quantities Measurement, Hubei Key Laboratory of Gravitation and Quantum Physics, PGMF, Huazhong University of Science and Technology, Wuhan 430074, People's Republic of China*

[2]*School of Mechanical Engineering and Electronic Information, China University of Geosciences, Wuhan 430074, People's Republic of China*

[3]*MOE Key Laboratory of TianQin Mission, TianQin Research Center for Gravitational Physics and School of Physics and Astronomy, Frontiers Science Center for TianQin, CNSA Research Center for Gravitational Waves, Sun Yat-sen University (Zhuhai Campus), Zhuhai 519082, People's Republic of China*

(Received 4 September 2023; accepted 22 March 2024; published 23 April 2024)

The temperature gradient effect (TGE) is an important disturbance source in the inertial sensor, the core payload of space gravitational wave detectors. The inertial sensor electrode, made of copper alloy with high thermal conductivity, is expected to achieve lower temperature gradient, but its outgassing characteristics need to be verified experimentally. In this work, we have developed a torsion pendulum and measured the TGE of the copper alloy electrode. The measurement results show that the upper limit of the outgassing effect of this copper alloy gravitational reference sensor is about 18.0 pN/K, and the total TGE is less than 30.2 pN/K at 293 K, which can be ignored in the application of gravitational wave detection. Our work reveals key physical properties associated with TGE and provides a viable alternative for specialized equipment applications in spaceborne gravitational wave detection missions and beyond.

DOI: 10.1103/PhysRevD.109.082001

The inertial sensor (IS) plays a pivotal role in space-based gravitational detectors, necessitating meticulous shielding of free-falling test masses (TM) to uphold pure geodesic motion. For the gravitational-wave detection mission such as LISA and TianQin, maintaining a residual acceleration noise to the level of 10^{-15} m/s^2/Hz$^{1/2}$ within the frequency range of 0.1 mHz–1 Hz is imperative [1–4].

Thermal induced noise, including temperature gradient effects (TGEs), is an important source of nonconservative force noise on the TM. The LISA design has a noise budget of 5×10^{-16} m/s^2/Hz$^{1/2}$ for temperature effects [5,6]. TianQin requires a lower level of nonconservative force noise than LISA, so the noise budget related to temperature effects needs to be further reduced. Compared to the LISA-like heliocentric missions, the TGE is a big challenge for TianQin-like geocentric orbit missions. To suppress thermal induced noise, extremely high requirements are put forward for temperature control around the TM, such as the early design of TianQin, which put forward a requirement of 5 μK/Hz$^{1/2}$ (at 6 mHz) for differential temperature control [1]. On the other hand, the characteristics of the electrode housing (EH) around TM, such as thermal conductivity and properties of outgassing, also require further research.

Because of its good thermal conductivity and low coefficient of expansion, molybdenum is used as the main material of the EH in LISA and LISA Pathfinder [7–9]. During the LISA Pathfinder mission, some glitches behaving as spikes were observed, which may have been caused by the gas burst from the pores in the tungsten gravity balance masses [10,11]. Similar to tungsten, molybdenum is also produced through powder metallurgy processes, so there may also be many pores in molybdenum EH that produce gas bursts [12]. To address this issue, copper alloy with superior thermal conductivity and lower porosity can be expected to achieve a lower TGE. This feature may be able to meet the requirements of TianQin and other extreme precision projects, such as the DECI-hertz interferometer Gravitational wave Observatory and Big Bang Observer [13–15].

Understanding and estimating TGE entail delving into the specific mechanisms and parameters, particularly the asymmetric outgassing effect, which remains unexplored with copper alloys. Key parameters such as activation temperature, flow prefactor, and correction factor are currently unknown. To evaluate the compliance of copper

*liuli157@hust.edu.cn
†zhouzb@hust.edu.cn

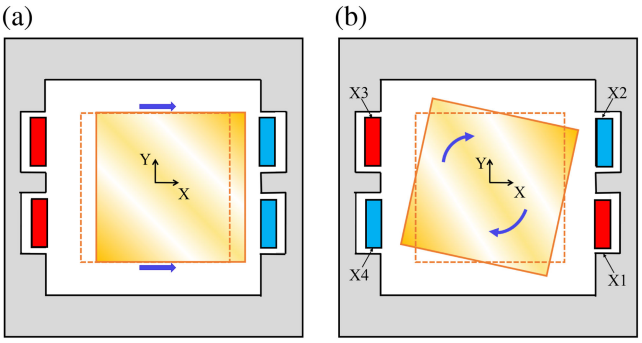

FIG. 1. Two modes of action for the TGE. (a) Transverse mode. (b) Diagonal mode.

alloy with TianQin requirements, experimental parameter measurements are conducted using a silica-fiber-suspension torsion pendulum. This study introduces a rotational-sensitive torsion pendulum facility to achieve TM free-fall conditions, with previous experience with torsion pendulum measurements [16–18].

Temperature gradient-induced force noise originates from the radiometer effect, radiation pressure, and temperature-dependent outgassing rates. For the TM in gravitational wave detection, TGE operates in two modes: transverse and diagonal, impacting TM translation and torsion dynamics, as depicted in Fig. 1. The transverse mode is characterized by TM translation due to temperature differences between electrodes X1 and X4 (or X2 and X3), while diagonal mode involves torques linked to temperature gradients across diagonal electrodes X1 and X3 (or X2 and X4).

The transverse force F in the transverse mode can be expressed as [19–21]

$$F = \kappa_{\mathrm{RM}} \frac{AP}{4T_0} \Delta T + \kappa_{\mathrm{RP}} \frac{8\sigma}{3c} A T_0^3 \Delta T + Q(T_0) \frac{A\Theta}{C_{\mathrm{eff}} T_0^2} \Delta T, \tag{1}$$

where κ_{RM} is a correction factors accounting for gas molecules incident on the Y and Z faces of the TM contributing a force along X. And $\kappa_{\mathrm{RM}} = 1$ would represent the case of two infinite parallel plates which is different with the realistic sensor geometry with finite dimensions. κ_{RP} is a correction factor accounting the TM reflectivity and radiation with a momentum component along X striking the Y and Z faces. c and σ are the speed of light in vacuum and the Stefan-Boltzmann constant, A is the area of one face of the TM, T_0 is the average temperature inside the EH, ΔT is the temperature difference along the x axis of TM, C_{eff} is the equivalent flow conductivity result from a combination of the conductance of the paths around the TM and through the holes in the gravitational reference sensor (GRS) EH, $Q(T_0) = Q_0 \mathrm{e}^{(-\Theta/T_0)}$, Θ and Q_0 are the activation temperature of gas molecules and the flow prefactor, respectively.

The torsion pendulum exhibits sensitivity to the torque imposed upon its TM, where the TGE becomes evident through both TM angle fluctuations and the subsequent damping oscillations encircling the suspension fiber.

The generated torque acting upon the rotational freedom can be expressed as

$$N = I\ddot{\theta} + \beta\dot{\theta} + k\theta, \tag{2}$$

where I denotes the TM's moment of inertia, β represents the damping coefficient of the torsion pendulum, k signifies the torsional stiffness, and θ stands for the TM's torsional angle. By employing Eq. (2), the torque of the torsion pendulum can be deduced through the differential and linear combination of the time series of twist angle. The torque N depends on pressure, average temperature, and temperature gradient. Consequently, the modulation of several parameters, including pressure, average temperature, and temperature difference, is requisite for their differentiation.

The torque N which causes the twist of pendulum includes the background torque N_0 due to stray force and torque on the TM, in addition to the TGE-induced action moment $N_{\Delta T}$, as captured in Eq. (3):

$$N = N_{\Delta T} \cdot \cos(\omega_{\Delta T} + \varphi) + N_0, \tag{3}$$

where $\omega_{\Delta T}$ designates the modulation frequency of the temperature gradient. If the temperature modulation is concentrated on the electrodes (only the four electrodes on the x axis are heated), the other surrounding areas of the EH contribute no TGE on the TM, then the TGE torque can be expressed as the combination of the forces from each electrode. Employing modulation and demodulation techniques, the $N_{\Delta T}$ can be extracted as

$$N_{\Delta T} = \left(\gamma_{\mathrm{RM}} \frac{P}{4T_0} + \gamma_{\mathrm{RP}} \frac{8\sigma}{3c} T_0^3 + Q_0 \mathrm{e}^{-\Theta/T_0} \frac{\Theta}{C_{\mathrm{eff}} T_0^2} \right) A_{\mathrm{e}} b_{\mathrm{e}} \Delta T_{\mathrm{e}}, \tag{4}$$

where γ_{RP} and γ_{RM} can be an analogy with the correction factors κ_{RP} and κ_{RM} introduced in Eq. (1) as the radiation pressure torque correction factor and radiometric torque correction factor for a finite-size sensor geometry. A_{e}, b_{e}, and ΔT_{e} are the effective area, the effective arm length, and the effective temperature difference, respectively. They are related to the sensor geometry and the temperature distribution inside the sensor.

Designating the four x-axis electrodes as X1, X2, X3, and X4 [refer to Fig. 1(b)], their respective temperatures are denoted as T_1, T_2, T_3, and T_4. When the electrodes X1 and X3 are heated, there is no direct heat conduction process between the electrodes and the surrounding area, and only a small thermal radiation effect. In a simplified model where we treat each electrode as isothermal, surrounding electrode housing surfaces as a uniform isothermal that is unaffected

by the electrode heating. Especially for the outgassing effect, we can assume that the outgassing phenomenon is uniform across the X electrodes surfaces. The torque transfer coefficient could be found by integrating the moment due to the differential pressure over the sensor surfaces. This would allow conversion between force and torque through an effective arm length $b_e = 1.20 \times 10^{-2}$ m, which is half of the center spacing of a pair of electrodes on the x axis. And $A_e = 1.13 \times 10^{-3}$ m^2 is the combined area of a pair of electrodes on the x axis. The effective temperature difference among the electrodes is defined as $\Delta T_e = (T_1 + T_3)/2 - (T_2 + T_4)/2$.

It is discernible from Eq. (4) that the three terms on the right side encompass the radiometer effect's action moment, radiation pressure effect, and asymmetric outgassing effect, respectively. The radiometer effect's moment can be further derived by modulating the pressure P. The radiation pressure effect and asymmetric outgassing effect are determined by the intercept of the linear fitting between $N_{\Delta T}$ and P.

The torsion pendulum employed for the terrestrial evaluation of TGE is presented in Fig. 2. The TM, weighing 60.5 g, is a hollow aluminum cube with dimensions of $50 \times 50 \times 50$ mm. Suspended by a 810 mm long, 40.4 μm diameter silica fiber, it is anchored to a magnetic damping stage used to suppress its swing mode. A 15 mm edge-length gold-coated glass cubic mirror is affixed to the TM and synchronously twisted with it. Monitoring the twist motion of the TM, an autocollimator with noise floor of

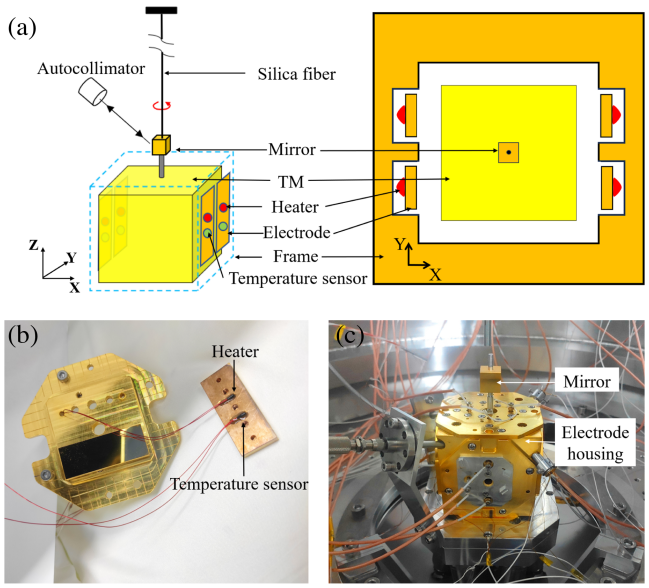

FIG. 2. Ground measuring device for the TGE. (a) Schematic diagram of the torsion pendulum. The TM is represented by the middle yellow cube in the structural diagram, and just the x axis is shown here around the surrounding electrodes. (b) The picture shows the way of installing the heater and temperature sensor. (c) Picture of the torsion pendulum used in this experiment.

0.2 μrad/Hz$^{1/2}$ is employed. The total suspending mass is roughly 84.9 g. The free twist period and Q factor of the pendulum are measured as 441(6) s and 1.3×10^4, respectively. Experimental outcomes reveal a torque sensitivity of 33 fNm/Hz$^{1/2}$ at 1 mHz.

The enclosing EH encompasses a housing frame and 18 electrodes: 12 sensing electrodes and 6 injection electrodes. The size of the X electrodes is 38.6×14.6 mm, the center distance between adjacent electrodes is 24.0 mm, and the gap between the X electrodes and TM is 4.7 mm. To avoid collision of TM on the electrodes, the gap between the housing frame and TM is 0.2 mm smaller than the gap between sensing electrodes and TM along each axis. Employing the material of copper alloy, both the electrodes and TM are gold coated to a thickness of 50 nm to enhance chemical stability. To centralize the TM within the EH, a high precision six-axis parallel positioner supports the housing frame.

Both heating and temperature measurement are performed by negative temperature coefficient thermistors [22]. The thermistors are attached directly on the back of the electrodes, which are mounted on the EH frame through glass spacers, as depicted in Fig. 2(b). This scheme can avoid the temperature of the EH frame from being affected by temperature gradient modulation, thereby improving the extraction accuracy of TGE parameters. The heating thermistors are endowed with a maximum power of 50 mW, establishing an effective temperature difference ΔT_e exceeding 1 K at room temperature, fulfilling experimental prerequisites. Developed by our group, the thermometer exhibits a noise level of 2×10^{-3} K/Hz$^{1/2}$ within the modulation frequency band.

The torsion pendulum resides within a vacuum chamber, offering adjustable pressure ranging from 1×10^{-6} Pa to 5×10^{-4} Pa through a flapper valve connected to a turbomolecular pump. Pressure measurements, subject to ±2% measurement error within the range of 2×10^{-10} Pa to 1×10^{-2} Pa, are facilitated via an extractor gauge (Leybold IE514 and CM52), and the measurement deviation introduced by the gas composition has been corrected with the measurement results of RGA. Enclosed within a temperature-insulated housing crafted from insulating material (phenolic foam board) in addition to the vacuum pump, the vacuum chamber can maintain an average temperature spanning 291–304 K through lab air conditioning. The experiment is performed at six distinct average temperatures: 293.0(1), 297.5(1), 297.9(1), 299.0(2), 299.5(1), and 301.1(1) K, and the temperature gradient modulation period is 2400 s.

Temperature difference modulation curves are depicted in Fig. 3(a), with an average temperature of 293.0(1) K. Over a measurement period of 12 hours, chamber pressure adjustments are implemented every 2 hours while temperature difference modulation persists. Each average temperature is examined over three consecutive days, and the

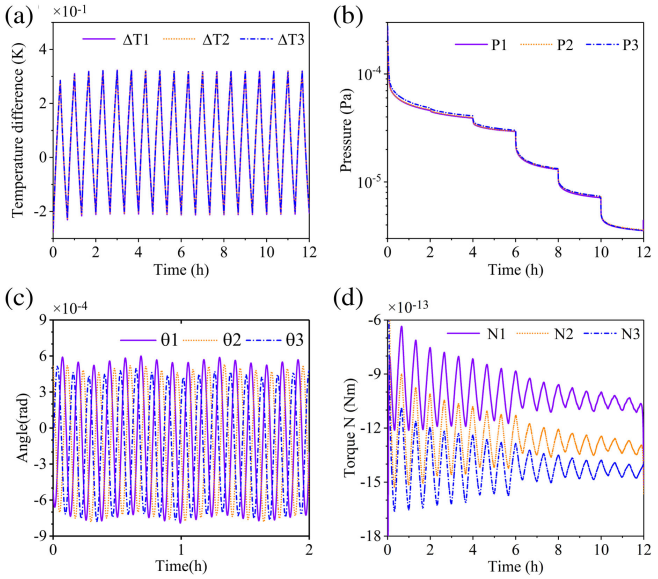

FIG. 3. (a) The temperature difference generated by modulation. (b) Adjusted pressure after changing the opening of the flapper valve every two hours. (c) The motion angle of torsion pendulum was measured by autocollimator. (d) The torque response of the torsion pendulum. As the pressure gradually decreases, the torque response gradually becomes smaller. The average temperature is 293.0(1) K.

numerical labels in Fig. 3 correspond to experiments conducted on days 1 through 3. The calibration of the relation between the chamber pressure and flapper valve opening is implemented prior to temperature modulation, permitting the exclusion of the vacuum gauge generating charged particles during modulation.

The pressure measurement results are displayed in Fig. 3(b). Gradually opening the flapper valve results in a gradual reduction in pressure. Following the change of valve conduction, pressure changes rapidly and then gradually reaches a stable value. The pressure data taken is the average of multiple measurements, with an error of less than 5%.

The related angle of the torsion pendulum throughout the modulation experiment is shown in Fig. 3(c). The torque on pendulum calculated from the angle time series is showcased in Fig. 3(d). Obviously the torque diminishes as chamber pressure decreases. For stable data extraction and estimate the TGE-induced torque $N_{\Delta T}$, only the data in the second modulating cycle are used. The mean pressure across three experiments [Fig. 3(b)] is portrayed in Fig. 4. Demodulating temperature difference and moment yield torque values under unit temperature difference (Fig. 4). The torque generated per unit temperature difference between a pair of x-axis electrodes can be determined using Eq. (4).

Moreover, we find that the value of $N_{\Delta T}/\Delta T$ is proportional to the pressure P at 293.0(1) K. Using the same method, we also obtained the relationship curve between them at other average temperatures, as shown in Fig. 5.

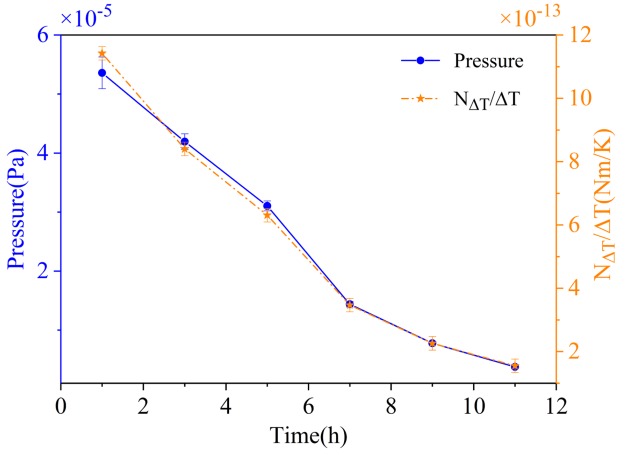

FIG. 4. Average value of modulate pressure and torque value per unit temperature difference. The average temperature is 293.0(1) K.

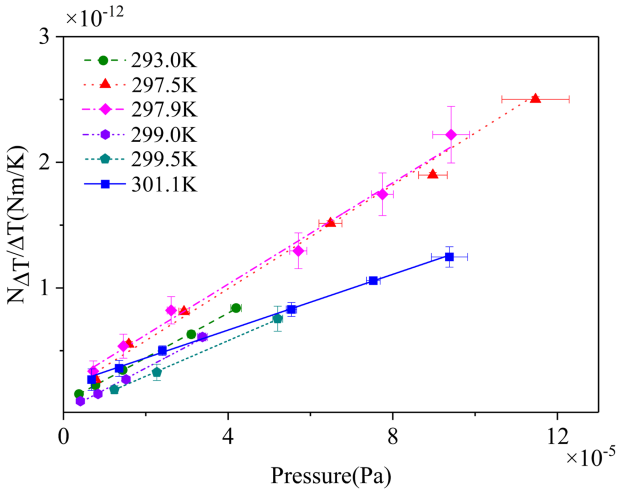

FIG. 5. Modulation experiments are performed at six different average temperatures. The vertical axis is the total torque of the TGE with per unit temperature difference.

To obtain the correction coefficient of the radiometer effect and the radiation pressure effect, we have performed a Monte Carlo simulation for our ground measuring IS geometry. Similar to the method described in Ref. [19], the basic principle is to simulate the noninteracting gas molecules (or photons) bouncing in the gap between the TM and the frame. In the presence of a temperature gradient along the housing, we can obtain the total force and torque on the TM for a given number of molecules. It should be noted that the temperature gradient in our simulation is set as illustrated in Fig. 1(b), which is slightly different from Ref. [19]. The corresponding torque correction factors are listed in Table I, with a statistical error of about 1%.

According to the slope of each curve in Fig. 5, we can get the torque correction factor of the radiometer effect, γ_{RM}. The experimental values at different average temperatures

TABLE I. Results of the torque correction factors simulations. Result for radiation pressure effect as shown for different values of the absorption a and nature of reflection (specular and diffuse).

γ_{RM}		1.18
γ_{RP}	$a = 1$	0.69
	$a = 0.05$, specular	0.16
	$a = 0.05$, diffuse	0.18

differ greatly, and the consistency between experimental values and simulation values is not very good, which is illustrated in Fig. 6 and which prevents a clear resolution of the expected $1/T_0$ effect. We suspect that the $1/T_0$ model of the radiometer effect may be too simple for our experiment. We will further consider the mechanisms between gas molecules and macroscopic objects (elastic collision and absorption-reemission cycle [18]) and its dependence of macroscopic object materials, modify the model, and design experiments to verify the model in the near future.

Then, we can obtain the zero-pressure values of the torque at different average temperature from the data in Fig. 5. As discussed above, these values are contributed from the radiation pressure effect and the outgassing effect. These two effects predict distinctly different temperature dependence. Because of the exponential-like temperature dependence predicted for outgassing, the radiation pressure effect is difficult to obtain from the experimental results directly. In order to study the asymmetric outgassing effect, the simulated thermal radiation pressure value is subtracted from the intercept.

The radiation pressure effect is particularly significant for the metallic surface of the electrodes and TM, which

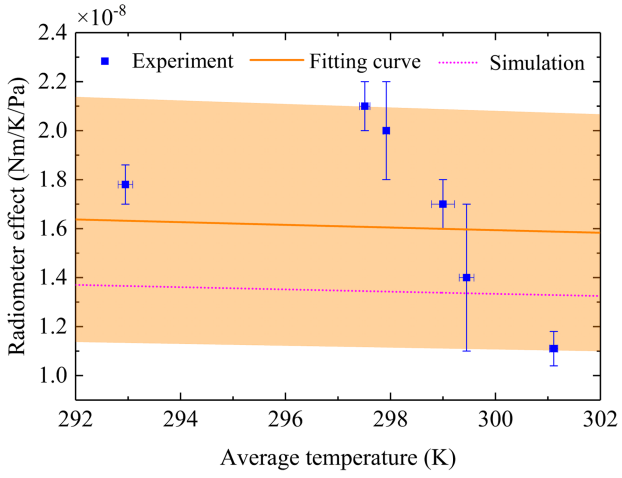

FIG. 6. Experimental measurements, fitting curves, and numerical simulations of the radiometer effect. The blue dots are experimental measurements at different average temperatures. The shadowed orange line is the fitting curve with errors. The pink dotted line is the numerical simulations values based on the γ_{RM} at Table I.

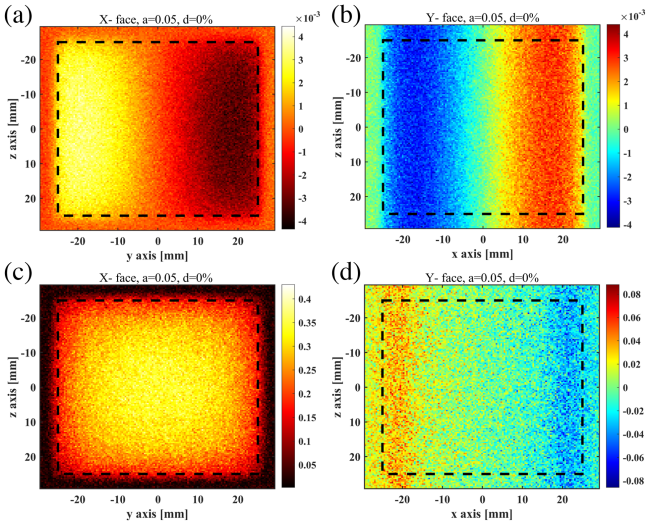

FIG. 7. Intensity plots of the torque coefficient (a), (b) and the force coefficient (c), (d), normalized by the factor $(2\sigma/3c)$, for emitting points on the X and Y surfaces. The outline of the TM section is shown as a dashed line 50 mm square in each case. The reflection properties: absorption coefficient $a = 5\%$, purely specular reflection ($d = 0\%$). Legends for the intensity values are shown in the color bars on the right of each plot.

are expected to have a high 95% ($a = 0.05$) reflectivities at thermal photon wavelengths and have specular reflection [23]. For the case of the high reflectivity surfaces of our IS—using $a = 0.05$, with specular reflection—there is a suppression of the radiation pressure effect, with $\gamma_{RP} = 0.16$. In addition, the intensity plots of the force coefficient and the torque coefficient, normalized by the factor $(2\sigma/3c)$, for emitting points on the X and Y surfaces are given in Fig. 7, respectively. The simulation results indicate a stronger suppression of the radiation pressure effect with a higher reflectivity surfaces.

Based on the simulation, the contribution of radiation pressure effect in our experiment is 27.5(3) fNm/K $(T_0/293\ \mathrm{K})^3$. After subtracting it from the intercept of each curve in Fig. 5, the outgassing effect at different average temperatures can be obtained, as shown in Fig. 8. Fitting multiple measurements at different average temperatures reveals an activation temperature Θ of approximately $2.07(2) \times 10^4$ K and a flow prefactor Q_0 of about $2.4(3) \times 10^{21}$ Pa m^3/s, where C_{eff} is a geometrical factor resulting from a combination of the conductance of the paths around the TM and through the holes in the GRS EH walls, estimated to be roughly 3.6×10^{-2} m^3/s by MolFlow + from the geometry parameters of TianQin IS [24,25]. These findings align with the established activation temperature range of 3000–30 000 K [5,26]. The average activation temperature is slightly increasing with time since particles with lower activation temperatures will be outgassed faster than those with higher activation temperatures [27].

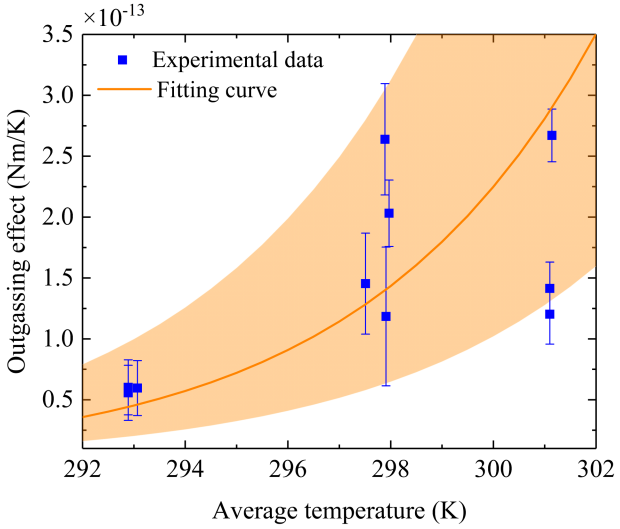

FIG. 8. Experimental measurements and fitting curves of the outgassing effect. The blue dots are experimental measurements at different average temperatures. The shadowed orange line is the fitting curve with errors.

In the experimental measurement, we also found that part of the torque produced by the outgassing effect is negative. This phenomenon may be due to the inhomogeneous outgasses and inhomogeneous temperature distribution of the EH around the TM. Exact values of Q_0 and Θ are difficult to predict on ground and will not be revealed until first measurements are taken on board the satellite. In space, the vacuum of GRS gradually gets better over time, and this phenomenon has been found in LPF [28,29]. At the same time, GRS in space applications are baked out at more demanding high temperatures. Therefore, we expect that the GRS made of copper-alloy material will have a smaller outgassing effect in space compared to the ground experiment results.

We also simulated the force correction coefficient of the radiometer effect and the radiation pressure effect from the geometry parameters of TianQin IS ($A_{\mathrm{TQ}} = 5\ \mathrm{cm} \times 5\ \mathrm{cm}$), which are listed in Table II.

According to Eq. (1), the TianQin TGE transfer function can be expressed (with $\kappa_{\mathrm{RM}} = 1.28$, $\kappa_{\mathrm{RP}} = 0.30$)

$$\begin{aligned}\frac{\mathrm{d}F}{\mathrm{d}(\Delta T)} = {} & 2.7\ \mathrm{pN/K} \times \left(\frac{P}{10^{-6}\ \mathrm{Pa}}\right)\left(\frac{293\ \mathrm{K}}{T_0}\right) \\ & +9.5\ \mathrm{pN/K} \times \left(\frac{T_0}{293\ \mathrm{K}}\right)^3 \\ & +8.4\ \mathrm{pN/K} \times \mathrm{e}^{-(2.07\times10^4)\left(\frac{293\ \mathrm{K}}{T_0}\right)}\left(\frac{293\ \mathrm{K}}{T_0}\right)^2. \end{aligned} \quad (5)$$

As can be seen from Eq. (5), the overall TGE-induced net force of per degree of temperature difference is 20.6 pN/K. The values of Q_0 and Θ here are the fitting values of the ground torsion pendulum experiment. For the "worst case" ($\Theta = 2.05 \times 10^4$ K and $Q_0 = 2.7 \times 10^{21}$ Pa m^3/s), the contribution of the outgassing effect will reach 18.0 pN/K, and the total TGE is reached 30.2 pN/K.

TABLE II. Results of the force correction factors simulations. Result for radiation pressure effect as shown for different values of the absorption a and nature of reflection (specular and diffuse).

κ_{RM}		1.28
κ_{RP}	$a = 1$	1.12
	$a = 0.05$, specular	0.30
	$a = 0.05$, diffuse	0.70

TABLE III. Reevaluation of TGE noise of TianQin IS assuming $\delta(\Delta T) = 5\ \mu\mathrm{K/Hz^{1/2}}$ at 6 mHz and $\delta(\Delta T) = 20\ \mu\mathrm{K/Hz^{1/2}}$ at 0.1 mHz.

Acceleration noise ($\mathrm{m/s^2/Hz^{1/2}}$)	Values at 6 mHz	Values at 0.1 mHz
a_{RM}	5.57×10^{-18}	2.23×10^{-17}
a_{RP}	1.94×10^{-17}	7.76×10^{-17}
a_{OG}	$\lesssim 3.76 \times 10^{-17}$	$\lesssim 1.50 \times 10^{-16}$
a_{Total}	$\lesssim 6.26 \times 10^{-17}$	$\lesssim 2.50 \times 10^{-16}$

By utilizing the experimental parameters, simulating parameters and the prescribed settings of the TianQin mission [1], we were able to estimate the total acceleration noise and individual component noise of the TGE. These results are summarized in Table III, revealing that current experimental measurements exhibit a magnitude better than the mission requirement (5.2×10^{-16} $\mathrm{m/s^2/Hz^{1/2}}$ at 6 mHz). Table III shows the acceleration noise of TianQin from TGE for the "worst case". Considering the temperature gradient control at lower frequency is more difficult, the TGE estimation at 0.1 mHz is also listed assuming the differential temperature fluctuation around the TM can achieve 20 $\mu\mathrm{K/Hz^{1/2}}$.

In this study, we have meticulously designed and implemented a suite of temperature-measuring and heating apparatus tailored for conducting TGE experiments. Furthermore, we have successfully constructed a dedicated ground test platform for the EH of the TianQin IS. Leveraging an EH prototype of copper alloy, we have conducted experimental evaluations to quantitatively assess the TGE's contribution. Our efforts encompassed an investigation into the outgassing effect coefficient of copper alloy, which included the determination of activation temperature and flow prefactor. These measurements provide critical insights into the behavior of these materials under specific conditions, contributing to our broader understanding of TGE mechanisms.

Evidencing its higher thermal conductivity, the material of copper alloy also manifests a more pronounced temperature evenness. As a corollary, its temperature gradient effect is poised to be comparatively reduced. These observations

collectively reinforce the advantageous role of the copper alloy in mitigating temperature-induced perturbations within sensitive systems. Conversely, the coefficient of expansion for the copper alloy exceeds that of molybdenum, resulting in more pronounced deformations under equivalent temperature variations. This characteristic renders the design of the EH's structural components more demanding when employing the EH of copper alloy.

In closing, this research not only advances our understanding of TGE phenomena but also contributes practical solutions and crucial data to elevate the performance of gravitational wave detection systems. As the field of precision measurement continues to evolve, our findings pave the way for enhanced instrumentation and improved models that ultimately advance our exploration of the space science.

This work was supported by the National Key R&D Program of China (Grant No. 2020YFC2200500), and the National Natural Science Foundations of China (Grants No. 12075092, No. 11975105, and No. 11727814).

[1] J. Luo *et al.*, Classical Quantum Gravity **33**, 035010 (2016).
[2] W.-T. Ni, Int. J. Mod. Phys. D **25**, 1630001 (2016).
[3] L. Carbone, A. Cavalleri, R. Dolesi, C. D. Hoyle, M. Hueller, S. Vitale, and W. J. Weber, Phys. Rev. Lett. **91**, 151101 (2003).
[4] P. Amaro-Seoane, H. Audley, S. Babak, J. Baker, E. Barausse, P. Bender *et al.*, arXiv:1702.00786.
[5] R. T. Stebbins, P. L. Bender, J. Hanson, C. D. Hoyle, B. L. Schumaker, and S. Vitale, Classical Quantum Gravity **21**, S653 (2004).
[6] L. Carbone, A. Cavalleri, R. Dolesi, C. D. Hoyle, M. Hueller, S. Vitale, and W. J. Weber, Classical Quantum Gravity **22**, S509 (2005).
[7] R. Dolesi, D. Bortoluzzi, P. Bosetti, L. Carbone, A. Cavalleri, I. Cristofolini, M. DaLio, G. Fontana, V. Fontanari, and B. Foulon, Classical Quantum Gravity **20**, S99 (2003).
[8] L. Carbone, G. Ciani, R. Dolesi, M. Hueller, D. Tombolato, S. Vitale, and W. J. Weber, Phys. Rev. D **75**, 042001 (2007).
[9] A. Cavalleri, G. Ciani, R. Dolesi, A. Heptonstall, M. Hueller, D. Nicolodi, S. Rowan, D. Tombolato, S. Vitale, P. J. Wass, and W. J. Weber, Phys. Rev. Lett. **103**, 140601 (2009).
[10] E. Castelli, Ph.D. thesis, University of Trento, 2020.
[11] M. Armano, H. Audley, J. Baird, P. Binetruy, M. Born, D. Bortoluzzi *et al.*, Phys. Rev. D **106**, 062001 (2022).
[12] J. Shields, *Application of Molybdenum Metal and Its Alloys* (The International Molybdenum Association, London, UK, 2013), ISBN 978-1-907470-30-1, https://www.imoa.info/download_files/molybdenum/Applications_Mo_Metal.pdf.
[13] N. Seto, S. Kawamura, and T. Nakamura, Phys. Rev. Lett. **87**, 221103 (2001).
[14] S. Kawamura *et al.*, Classical Quantum Gravity **28**, 094011 (2011).
[15] G. M. Harry, P. Fritschel, D. A. Shaddock, W. Folkner, and E. S. Phinney, Classical Quantum Gravity **23**, 4887 (2006).
[16] H.-B. Tu, Y.-Z. Bai, Z.-B. Zhou, L. Liu, L. Cai, and J. Luo, Classical Quantum Gravity **27**, 205016 (2010).
[17] H. Yin, Y.-Z. Bai, M. Hu, L. Liu, J. Luo, D.-Y. Tan, H.-C. Yeh, and Z.-B. Zhou, Phys. Rev. D **90**, 122001 (2014).
[18] Y.-J. Zhao, G.-L. Li, L. Liu, C.-G. Shao, D.-Y. Tan, H. Yin, and Z.-B. Zhou, Phys. Rev. Appl. **19**, 044005 (2023).
[19] L. Carbone, A. Cavalleri, G. Ciani, R. Dolesi, M. Hueller, D. Tombolato, S. Vitale, and W. J. Weber, Phys. Rev. D **76**, 102003 (2007).
[20] A. Cavalleri, G. Ciani, R. Dolesi, M. Hueller, D. Nicolodi, D. Tombolato, P. J. Wass, W. J. Weber, S. Vitale, and L. Carbone, Classical Quantum Gravity **26**, 094012 (2009).
[21] F. Rivas, Ph.D. thesis, University of Barcelona, 2019.
[22] G. Ciani, Ph.D. thesis, University of Trento, 2008.
[23] Y. S. Touloukian and D. P. DeWitt, *Thermal Radiative Properties: Metallic Elements and Alloys, Thermophysiscal Properties of Matter*, The TPRC Data Series Vol. 7 (IFI/Plenum, New York, 1970), pp. 244–245.
[24] R. Kersevan and J. L. Pons, J. Vac. Sci. Technol. A **27**, 1017 (2009).
[25] R. Kersevan and M. Ady, in *10th International Particle Accelerator Conference, Melbourne, Australia* (JACoW Publishing, Geneva, Switzerland. 2019), TUPMP037, ISBN 978-3-95450-208-0, https://doi.org/10.18429/JACoW-IPAC2019-TUPMP037.
[26] A. Rüdiger, Residual gas effect in space-born position sensors, MPI für Gravitationsphysik (AEI Hannover) (2002) (unpublished), http://eotvos.dm.unipi.it/opendiscussion/ruediger_30aprile.pdf.
[27] F. Gibert, Ph.D. thesis, Universitat Politècnica de Catalunya, 2015.
[28] M. Armano, H. Audley, J. Baird, P. Binetruy, M. Born, D. Bortoluzzi *et al.*, Phys. Rev. Lett. **120**, 061101 (2018).
[29] M. Armano, H. Audley, G. Auger, J. Baird, M. Bassan, P. Binetruy *et al.*, Phys. Rev. Lett. **116**, 231101 (2016).